

Hydrogen-enhanced oxidation of ferrite phase in stainless steel cladding and the contribution to stress corrosion cracking in deaerated high temperature water

Tongming Cui^{a,b}, Haiying Dong^{a,b}, Xinhe Xu^{a,b}, Jiarong Ma^{a,b}, Zhanpeng Lu^{a,b,*}, Yuanjie Tang^{a,b}, Deng Pan^{a,b}, Sergio Lozano-Perez^c, Tetsuo Shoji^d

- a. Institute of Materials, School of Materials Science and Engineering, Shanghai University, Shanghai, 200072, China
- b. State Key Laboratory of Advanced Special Steel, Shanghai University, Shanghai, 200072, China
- c. Department of Materials, University of Oxford, OX1 3PH, Oxford, UK
- d. New Industry Creation Hatchery Center, Tohoku University, Sendai, 980-8579, Japan

*Corresponding author, zplu@t.shu.edu.cn

Abstract

Oxide film properties and stress corrosion cracking (SCC) behaviour are investigated in the 308L stainless steel cladding layer with and without being H-charged in a deaerated high temperature water. Phase boundary (PB) has lower oxidation resistance than austenite and δ -ferrite matrix. A compact and high Cr content-bearing inner oxide layer improves the oxidation resistance of the δ -ferrite phase without H charging. H-induced PB penetration oxidation and grain boundary (GB) preferential oxidation are observed in H-charged specimen due to the PB and GB act as H trapping sites. Charged H decreases the oxidation resistance of δ -ferrite and austenite. δ -Ferrite acts as a path for H diffusing and H flux facilitates mass transport, resulting in the poor oxidation resistance of δ -ferrite. The mechanism underlying the effect of H on the oxidation behaviours of δ -ferrite and austenitic phases, as well as SCC performance, are discussed.

Keywords: Stainless steel, ferrite, hydrogen, oxidation, stress corrosion cracking, high temperature water

1. Introduction

In pressurized water reactor (PWR) systems, nominally austenitic stainless steels (SS), which contain a certain amount of ferrites, are cladded onto the reactor pressure vessel steel, the low alloy steel (LAS) nozzle portion in the dissimilar weld, and other components as an

isolation barrier between the low alloy steel and the primary water environments [1–6]. The compositions of austenitic weld metals are typically opted to promote primary solidification as δ -ferrite and a solid-state transformation to austenite to prevent hot cracking during the cladding process [2,7]. The as-cladded microstructure often retains some volume percentages of the body-centered cubic (bcc) ferrite phase at room temperature, leading to a duplex austenitic-ferritic microstructure [8]. The stainless-steel claddings are exposed to the primary loop water, and thus their resistance to corrosion and environmentally assisted cracking, including stress corrosion cracking (SCC) and corrosion fatigue, is vitally important. SCC is a local damage process and SCC crack-tips have been characterized and modeled to understand the local damage mechanisms [9–16]. Dissolved hydrogen gas in a PWR's primary water environment can be absorbed on the alloy surface and decompose to atomic hydrogen, which can penetrate into the alloy matrix. It has been reported that hydrogen entry in the alloy substrate can influence the properties of the oxide film developed on metal or alloy surfaces [17–22].

In various alloy/solution systems, interplays between dislocations at a crack tip as a result of crack tip plasticity and hydrogen can play a crucial role in SCC [23–26]. In high-temperature water environments with low dissolved oxygen concentrations, the reduction of hydrogen ions or water is the main cathode reaction, and the resultant atomic hydrogen atoms can be absorbed by the fresh metal at the crack tip [27]. Some research results indicated that hydrogen can preferentially diffuse and accumulate ascribe to plastic deformation or a high stress/strain field in the crack tip zones [28–34]. Applied strain enhanced hydrogen accumulation and entering in the alloy matrix, this process has a promoting effect on the localized oxidation nucleation and crack initiation [33]. Beachem suggested the hydrogen-enhanced localized plasticity mechanism based on the theory that hydrostatic stress or the entry of hydrogen facilitates the dislocation motivation and the local plastic deformation at the crack tips [35]. Hydrogen would influence many factors, such as oxidation kinetics, electrochemical potential, pH, hydride formation and mechanical properties in the vicinity of a crack tip. Studying the effect of hydrogen on the corrosion reaction at crack tips is important for understanding the controlling factors of SCC. For SCC in high-temperature aqueous solution, the property of the oxide films is thought to play a critical role in the

cracking process [10,14–16].

In the present work, prior electrochemical H-charging has been used to cause a high H concentration in 308L SS cladding and simulate regions of high-susceptibility where H could reach higher concentrations, e.g. crack tips. Non-charged specimens and H-charged specimens are exposed and slow strain rate tensile (SSRT) tested in deaerated high temperature water, with the aim of revealing the effect of H on the oxidation behaviours of the austenite and δ -ferrite phases in 308L SS cladding and the implication on SCC performance.

2. Experimental procedures

2.1. Materials and microstructure characterization

A block with 308L SS clad on pressure vessel LAS was used in the experiments. The chemical composition of the 308L SS cladding was as follows (in wt.%): 0.03C, 0.89Si, 1.86Mn, 0.046Cu, 0.002S, 0.001Nb, 0.097Mo, 10.27Ni, 19.54Cr and Fe balance. The red box in Fig. 1a indicates the sampling position where the small pieces of 308L SS were obtained. The samples were cut with a dimension of 15 mm \times 10 mm \times 3 mm for microstructure analysis and immersion tests. Prior to the microstructural analysis and exposure tests, the specimen surfaces were ground up to 2000# with SiC waterproof papers, and then mechanically polished with a 1 μ m diamond suspension. Fig. 1b shows the surface morphology of 308L SS after electro-etched in a 40% NaOH solution for 30 s with a DC of 4 V, showing that the island-like ferrite distributed in the austenite substrate. The chemical composition of the ferrite was analyzed with an Apollo 300 scanning electron microscope (SEM), operated at 15 kV, equipped with an energy dispersive spectrometer (EDS) detector. Fig. 2 shows the SEM-EDS area maps and the element line profile of the δ -ferrite in 308L SS cladding. The higher chromium-concentration and lower nickel-concentration in δ -ferrite than that in austenite matrix.

2.2. Hydrogen-charging and exposure tests in high-temperature water

The electrode detail was described in our previous work [36]. Electrochemical hydrogen-charging was conducted under a constant cathodic current density of -2 mA/cm² in 0.5 mol/L H₂SO₄ containing 0.3 g/L thiourea (CH₄N₂S) for 24 h at room temperature. The

distance between the platinum sheet (counter electrode) and specimen (working electrode) was approximately 10 mm. The lattice diffusivity of hydrogen in the austenitic phase (γ) at room temperature was approximately $1.8\text{--}8\times 10^{-12}$ cm²/s [31,37], while in the ferrite phase (α) it was approximately 1.5×10^{-7} cm²/s [37]. In this study, the ferrite phase of the 308L SS cladding was δ -ferrite, so the diffusivity of hydrogen between α -ferrite and δ -ferrite should not make much of a difference. One can assume that the transport of hydrogen through the 308L SS occurs mainly through the ferrite matrix. The diffusion depth (χ) of hydrogen can be calculated by Eq. (1) [38]. The average diffusion depth of hydrogen from one side of the 308L SS specimen after hydrogen pre-charging for 24 h is estimated to be 8.67 μm in the austenite phase (γ), while in the ferrite phase (δ) it is approximately 26.83 μm .

$$\chi = \sqrt{2D_H t} \quad (1)$$

After hydrogen-charging, the specimen surfaces were cleaned with distilled water and ethanol, then exposed in a deaerated high temperature water environment containing 1200 mg/L of B as H_3BO_3 and 2.2 mg/L of Li as $\text{LiOH}\cdot\text{H}_2\text{O}$, which was prepared using analytical grade reagents and ultra-pure water. Prior to the elevated temperature and immersion tests, dissolved oxygen (DO) was removed from the test solution by means of bubbling purging gas N_2 ($\geq 99.999\%$) through the autoclave at a flow speed of 0.1 L/min for 1 h. The entire experimental process was under the conditions of 290 °C and ~ 7.1 MPa for 168 h and 600 h in a 2 L Ti-cladded static autoclave. For the 168 h immersion period, the hydrogen-free 308L SS was denoted as 308-168N, the hydrogen-charged 308L SS was denoted as 308-168H. For the 600 h immersion period, the hydrogen-free 308L SS was denoted as 308-600N, the hydrogen-charged 308L SS was denoted as 308-600H.

2.3. SSRT tests in high-temperature water

Prior to SSRT tests, the electrochemical hydrogen-charging was conducted under a constant cathodic current density of -5 mA/cm² in 0.5 mol/L H_2SO_4 containing 0.5 g/L $\text{CH}_4\text{N}_2\text{S}$ for 24 h at room temperature. The hydrogen-charged 308L SSRT specimen was denoted as 308-SH, the hydrogen-free 308L SSRT specimen was denoted as 308-SN. The 308L SS cladding specimens were extended at a strain rate of 3×10^{-7} /s. All the SSRT samples had a gauge dimension of 15 mm (length) \times 4 mm (width) \times 2.2 mm (thickness). The solution

for the SSRT tests in a 316 SS autoclave with equipment a water circulation loop was the same as the exposure tests. The pressure and temperature of the SSRT tests were 13.3 MPa and 325 °C, respectively. Before SSRT tests, the sample sides were polished using SiC waterproof papers up to 1500 # grit, subsequently cleaned with ultra-pure water and ethanol.

2.4. Characterization of the oxide films and fracture surfaces

Oxide phase analysis was conducted using an 18 kW D/Max 2500 X-ray diffraction (XRD) analyzer with a Cu K alpha X-ray source, operating at 40 kV. The XRD 2 θ scan range was from 20° to 70° with a 2°/min scan speed at the step size of 0.02°. The oxide film surface morphologies were observed via an FEI Helios 600i Nanolab SEM operated at 10 kV. For a cross-sectional transmission electron microscopy (TEM) analysis, the lamellar samples containing the oxide film and matrix were prepared using an FEI Helios Nanolab 600i focused ion beam (FIB) system. The oxide film cross-sectional elemental composition and microstructure were analyzed using JEM-2100F TEM and Talos F200X G2 TEM with energy-dispersive X-ray spectroscopy (EDX), operating at 200 kV. The fast Fourier transformation (FFT) images were gained from the high-resolution TEM (HRTEM) images. High-angle annular dark-field (HAADF) photographs were obtained in the scanning TEM (STEM) mode. The SEM fractographs of the 308-SN and 308-SH specimens were acquired via an Apollo 300 thermal-field emission SEM with a voltage of 15 kV.

3. Results

3.1. Properties of the oxide films after exposure for 168 h and 600 h

[Fig. 3](#) shows the XRD patterns of the oxide film developed on 308L SS with and without charged-hydrogen after being exposed to deaerated high temperature water at 290 °C for 168 h and 600 h. The oxide films were grown on both the H-charged and H-free specimens mainly show the characteristic peaks of chromia and magnetite oxide structure.

[Fig. 4](#) shows the SEM images of the oxide films and ferrites cross-sectional of 308-168N and 308-168H specimens. The oxide particles formed on the surface of the 308-168N specimen are dispersed and discontinuous, and the size of the oxide particles is inhomogeneous, as shown in [Fig. 4](#) a and b. The ferrite in 308-168N has not occurred local denting oxidation, as shown in [Fig. 4](#) c. In the 308-168H specimen, the local denting

oxidation appears on the ferrites, and the number of the oxide particles upon the H-charged 308-168H sample tends to be greater than that upon the H-free 308-168N sample, as shown in Fig. 4 d and e. H-induced the in-depth ferrite matrix defect is observed in 308-168H specimen, as shown in Fig. 4 f.

TEM-EDS results from the cross-sectional specimen containing the oxide film formed on austenite of the 308-168N specimen, as shown in Fig. 5. The oxide film exhibits a double-layer structure, with the non-stoichiometric $\text{Fe}_x\text{Cr}_y\text{Ni}_z\text{O}_4$ oxide in the outer oxide film and the chromium-rich oxide in the inner oxide film. Nickel is accumulated at the oxide/austenite matrix (O/AM) interface and grain boundary (GB), accompany by depleted in Cr. The thickness of the Cr-rich inner oxide layer grown on austenite of 308-168N specimen is about 15 ± 5 nm. Fig. 6 shows the TEM results of the sampling location of the phase boundary (PB) and the oxide film formed on 308-168N specimen. The Cr-carbides are distributed semi-continuously along the phase boundaries. The ferrite has not occurred local denting oxidation. The thickness of the inner oxide layer grown on ferrite measured by TEM is about 5 ± 2 nm, as shown in Fig. 6c. Preferential oxidation of PB is observed, and the oxide adjacent to the PB seems not compact with some voids, as shown in Fig. 6b and d. The inner layer oxide and the oxidized PB are Cr-rich oxides. Ni is enriched in the oxide/ferrite matrix (O/FM), O/AM and oxide/carbides interfaces.

TEM-EDS results from the cross-sectional specimen containing the oxide film formed on austenite of the 308-168H specimen, as shown in Fig. 7. The oxide film exhibits a double-layer structure, with large and loose Fe-rich oxide particles distribute in the outer layer and a dense inner layer mainly consisting of Cr-rich oxides, as shown in Fig. 7 area maps. The Fe content in the outer layer oxide on 308-168H is higher than that on 308-168N (see Figs. 5c and d, 7c and d). The thickness of the Cr-rich inner oxide layer formed on austenite of 308-168H specimen is about 90 ± 10 nm. Fig. 8 shows the TEM-EDS results of the sampling location of the PB and the oxide film formed on 308-168H. H accelerates oxidation of the ferrite, and the penetration oxidation of the PB is observed in the 308-168H specimen. The oxidized PB and ferrite matrix are mainly Cr-rich oxide and Fe-rich oxide, respectively. The Cr in the ferrite matrix may be diffusion to the PB and oxide/solution interface during exposure in high-temperature water.

Fig. 9 shows the SEM images of the oxide films and ferrites cross-sectional of 308-600N and 308-600H specimens. It can be seen that the surface of 308-600N specimen is covered by polyhedral oxide particles, and no local denting oxidation has been occurred in the ferrite, as shown in Fig. 9a-c. The oxide particles formed on the 308-600H specimen surface are relatively compact and continuous. Similar to 308-168H specimen, the local denting oxidation and H-induced the in-depth ferrite defect that appeared on the ferrites in the 308-600H specimen, as shown in Fig. 9d-f.

Fig. 10 and 11 show the TEM results of the sampling location of the PB and the oxide film formed on the 308-600N specimen. Local denting oxidation of ferrites is not significant. The carbides are distributed semi-continuously along the phase boundaries. Evidence of preferential oxidation on the ferrite side at the phase boundaries indicates that galvanic oxidation has occurred, with the ferrite likely to provide some form of cathodic protection to the austenite [39]. A continuous Ni-rich region close to the O/FM interface is observed, as shown in the area maps of Fig. 10a. The Cr-depletion at the phase boundary is observed in Fig. 10b. The thickness of the Cr-rich inner oxide film formed on ferrite is approximately 20 nm thinner than that on austenite (approximately 90 nm), as shown in Fig. 10c-f. Furthermore, the average Cr content in the inner oxide film on ferrite (~ 42 wt.%) is higher than that on austenite (~ 34 wt.%), as shown in Fig. 10d and f, which might have led to more efficient passivation, given the oxide is thinner. The SAED pattern I reveals the “fish-like” shape ferrite matrix is bcc structure, as shown in Fig. 11a. The SAED pattern III reveals the carbide is Cr_{23}C_6 , as shown in Fig. 11b. The SAED pattern II of the outer layer oxide, as indicated in Fig. 11b, shows the presence of the Fe_3O_4 -type crystal structure, and the bright diffraction ring from the FFT of the internal oxide film shows the presence of $(\text{Fe}_x\text{Ni}_{1-x})\text{Cr}_2\text{O}_4$ and Cr_2O_3 in pattern IV of Fig. 11.

Fig. 12 shows the TEM results of the sampling location of the GB and the oxide film formed on the austenite of the 308-600H specimen. The double oxide layers are observed, with an outer Fe-rich oxide and an inner Cr-rich oxide. An intergranular carbide protrudes above the O/AM interface due to its slower corrosion rate. Below, the GB began oxidizing preferentially. It can be seen that Ni is enriched ahead of the oxidation front of GB. Kruska et al. [40] thought that Ni enrichment could stop or at least delay further oxygen diffusion

along with the GB. The thickness of the internal oxide layer grown upon austenite of 308-600H sample is approximately 120 ± 10 nm. The lattice structure of the outer and inner oxide layer determined by the SAED pattern (Fig. 12c, regions II and III) are magnetite-type spinel oxide and chromium-rich nanocrystalline, respectively.

Fig. 13 and 14 show the TEM results of the different sampling locations of the PB and the oxide film formed on the 308-600H specimen. The oxide film formed on austenite and ferrite is a double-layer structure, with Fe-rich in the outer layer and Cr-rich in the inner layer. Cr-carbides along the phase boundaries, Ni-enrichment at the O/FM interface, uneven oxidation of the ferrite phase, and preferential oxidation occurred at the PB on the ferrite adjacent to the austenite are observed, as shown in Fig. 13a and b. The SAED patterns I and II reveal the ferrite and austenite matrix are bcc and face-centered cubic (fcc) structures, respectively. The SAED pattern III from the outer layer oxide shows the Fe_3O_4 -type spinel structure. The SAED pattern IV and V from the inner layer oxide on ferrite show the diffraction rings, which indicates the presence of mixed oxides: $(\text{Fe}_x\text{Ni}_{1-x})\text{Cr}_2\text{O}_4$ spinel and Cr_2O_3 . The average thickness of the inner oxide film on ferrite measured by TEM was 180 ± 30 nm, as shown in Fig. 14a and b.

3.2. SSRT test results

Fig. 15 shows the engineering stress-strain curves of the 308-SN and 308-SH samples after SSRT test at strain rate of 3×10^{-7} /s in deaerated high temperature water at 325 °C. The ultimate tensile strength (UTS) of the 308-SN and 308-SH specimens is 451 MPa and 397 MPa, respectively. The yield strength (YS) of the 308-SN and 308-SH specimens is 210 ± 5 MPa and 215 ± 5 MPa, respectively. The elongation to fracture is 58.6% for 308-SN specimen and 49.4% for 308-SH specimen. The results show that pre-charged hydrogen significantly decreases the elongation to fracture and UTS, but the YS has no apparent change.

Fig. 16 shows the SEM fractographs of the 308-SN specimen after SSRT test at 3×10^{-7} /s in deaerated high temperature water at 325 °C. The fracture surface is not smooth. Some large holes are distributed on the fracture surface, which may be ascribed to the stripping of the inclusions from the metal matrix, as shown in Fig. 16c. The fracture surface for 308-SN exhibits ductile characteristics by evidence of the shear dimple and normal dimple; the normal dimples include dimple 1 and dimple 2 (fine equiaxed dimples), as shown in Fig.

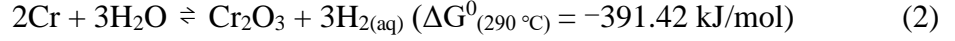
16b and d. There is no obvious SCC indication in the fracture zones. The gauge side surface of 308-SN shows that the slightly necking occurs in the specimen, and the cracking mode is transgranular (TG) in terms of the amounts of tearing-like cracks distribute on the side.

Fig. 17 shows the SEM fractographs of the 308-SH specimen after SSRT test at 3×10^{-7} s in deaerated high temperature water at 325 °C. The fracture surface topography of the 308-SH is smoother than that of the 308-SN, and no apparent necking occurred in the sample, as shown in Fig. 17a and e. It can be found that the intergranular (IG) cracking region is mainly distributed near the fracture edge with the brittle cracking between the dimple and IG cracks, as shown in Fig. 17a-d. The gauge side surface is covered by oxide particles and distributed different size IG cracks, as shown in Fig. 17e and f. Pre-charged hydrogen significantly increases the SCC susceptibility of the 308L SS cladding in a deaerated high temperature water environment.

4. Discussion

4.1. Oxidation behaviours of austenite and ferrite without H

In the H-free specimen, the oxide films formed on austenite and ferrite are a double-layer structure, as schematic in Fig. 18a. The growth of the outer oxide layer should occur via base metal dissolution and depend on Fe, Cr and Ni oxidation kinetics [22]. The inner oxide layer formed on the δ -ferrite is thinner than that on the austenite, indicating a higher oxidation resistance of δ -ferrite than that of austenite. The oxidation rate of SS in high-temperature water is mainly determined by the Cr-content in the SS matrix and the inner oxide film. If metallic diffuse through an interstitial site, it is reasonable to think that the diffusion of Cr in the bcc lattice (density $K=0.68$, 32% interstitial volume) is easier than that in the fcc lattice (density $K=0.74$, 26% interstitial volume) at elevated temperatures. Due to the diffusion-based process controls the oxidation rate, the higher content and lattice-diffusing coefficient of Cr in δ -ferrite (open lattice structure) than that in γ -austenite (close packed lattice) would cause a considerable flux density of chromium to outward transport [41-44]. In other words, it would facilitate the reaction of Eq. (2), resulting in a higher Cr-bearing oxide film grown upon δ -ferrite than upon γ -austenite during the early stage oxidation in high-temperature water.



The preferential oxidation of PB would be due to the chromium depletion at the δ/γ interface (see Fig. 10b) or local strain accumulation at this region [45], which is caused by the formation of Cr-rich δ -ferrite [46] or carbides [45,47]. Also, the low Cr content at the PB is insufficient to form the protective oxide film, therefore favoring the generation of the voids within the oxidized area (Fig. 6).

4.2. H-modified oxidation behaviours of austenite/ferrite, PB and GB

Charged hydrogen in metal or alloy distributes as a solid solution state at some trapping sites. At elevated temperature, the reduction of the activation energy needed for H escape from the trapping sites, thereby generating a highly H flux density (J_H) through the metal/oxide/water interface, which can be expressed as [31]:

$$J_H = -D_H \cdot (\nabla C)_t \quad (3)$$

where $(\nabla C)_t$ is the concentration gradient at a specific time t .

In the early stage of oxidation in high temperature water, a large amount of hydrogen diffusing from the metal matrix to the oxide film/water interfacial. The diffusing H would accelerate the mass transport process and cause a considerable defect in the oxide film, results in more cations being released from the metal to the outside. The larger oxide particles with higher Fe and thicker inner oxide on H-charged specimen (308-168H) than that on H-free specimen (308-168N) are evidence of this (Figs. 4,5 and 7). H decreases the oxidation resistance of ferrite and austenite, especially the ferrite, such as local denting oxidation occur in ferrite (Figs. 4,8,9,13 and 14). It has been reported that hydrogen has a lower diffusivity and a higher solubility in the austenite lattice than that in the ferrite lattice [31]. The diffusion process of hydrogen should include two parts: internal diffusion and external diffusion. The gap between the discontinuous carbides along with the PB would serve as a channel for internal hydrogen diffusion, the driving force of which is provided by the concentration gradient (∇C_H) between austenite and δ -ferrite, as shown in Fig. 18b. Since the ferrite phase acts as a fast outward diffusion path for hydrogen, the enhanced metal cations outward transport should occur in the ferrite phase. The H-induced defect/damage in ferrite phase should be larger than that in austenite phase. These defects/damage of the ferrite would not recover after the early period of 168 h and 600 h exposure tests. H-induced preferential

oxidation of GB and penetration oxidation of PB, are observed in the H-charged specimen, which may be due to the following three reasons: (i) the GB and PB always act as H traps, H-induced volume expansion ($v_H \approx 3\text{\AA}^3/\text{H atom}$) [48] to facilitate the vacancy and nanovoids formation. (ii) the hydrogen-enhanced decohesion decrease the bond force of the γ/γ and δ/γ interfaces (see Fig. 9f). (iii) H dissolved in these locations increases the chemical activity [49], thus favoring the early stage of oxidation initiation.

4.3. H-assisted SCC behaviour of 308L SS cladding

H-assisted SCC of the austenitic SS was reported previously [50,51]. Depending on combinations of metal/environment/loading conditions for SCC systems, crack initiation and growth are determined by the crack tip mechanical field, oxidation rate kinetics as well as film degradation or rupture parameters. Based on the synergism of crack tip strain rate and quasi-solid state transient oxidation kinetics [15,16,52-55], the crack growth rate of an alloy in high-temperature water can be expressed as

$$\frac{da}{dt} = k_a \cdot (\dot{\epsilon}_{ct})^m \quad (4)$$

$$\dot{\epsilon}_{ct} = \epsilon_d/t_d \quad (5)$$

where $\dot{\epsilon}_{ct}$ represents crack tip strain rate, k_a represents crack tip oxidation rate constant, ϵ_d represents threshold strain for degradation of the protective film, t_d represents the period of crack tip film degradation, m represents the slope of the oxidation rate decay curve.

The k_a can be expressed as Eq. (6) if using the parabolic oxidation kinetics based on solid-state oxidation mechanism [15,16,54-56].

$$k_a = [(k_1)^{(1-m)} \cdot (\epsilon_d)^{(-m)}] \quad (6)$$

where k_1 is the oxidation rate constant. Then Eq. (4) can be written as

$$\frac{da}{dt} = [(k_1)^{(1-m)} \cdot (\epsilon_d)^{(-m)}] \cdot (\dot{\epsilon}_{ct})^m \quad (7)$$

According to the modeling Eqs. (4)-(7), increasing oxidation rate constant k_1 or decreasing ϵ_d would lead to the increasing of SCC propagation rate. H-assisted δ -ferrite local denting oxidation causes the discontinuous oxide film on the metal surface, therefore decreasing the protective nature of the oxide film. In other words, H significant accelerates oxidation of the ferrite phase or H-induced oxide film defect, e.g., microcracks [22], would

decrease the ε_d . The oxidation rate constant k_1 increases as evidence by the thicker oxide layer on the H-charged sample than the H-free sample. Also, in the process of the SSRT, the H-induced preferential oxidation of GB and H-induced damage/defect of ferrite (e. g. the volume expansion, lattice distortion, local denting oxidation) would provide the preferential sites for stress corrosion cracks initiation. Moreover, the strain-induced H accumulated at the crack tip would promote the cracking process.

The different GBs would have different crack susceptibility with H. The GB types of the 308L SS cladding were mainly random grain boundaries (RGBs), the RGBs would more susceptible to cracks initiation than that of the coincidence site lattice (CSL) grain boundaries. It was reported that the RGBs were more susceptible to blistering than the CSL grain boundaries. H-charging can cause high strain levels and plastic deformation around the RGBs, but had no significant effect on the CSL grain boundaries [57]. The cracking mechanism of the H effects on the GBs types of the austenitic SS in high temperature water still needs to be further investigated. The results presented in this study suggest that H affects the oxidation behaviour of the austenite and δ -ferrite phases, PB, GB, as well as the SCC performance in weld-overlay claddings. The implications of these findings for in-service components in PWRs are relevant since they highlight the differences in oxidation resistance when extra H is present. This is likely to be the case for regions of high-defect density, e.g. grain boundaries, heat-affected zones, highly cold-worked regions, or more importantly, crack tips. Stress alone might not be accountable for the different oxidation behaviour (phase, oxide quality, dimensions) observed around crack tips, with H likely playing an important role that needs to be better addressed mechanistically.

5. Conclusions

The properties of the oxide films grown on 308L SS cladding with and without H-charging after exposure in deaerated high temperature water at 290 °C were characterized. The SCC susceptibility of the non-charged and H-charged 308L SS cladding was studied by SSRT tests. The main conclusions are as follows:

1. The oxide films formed on γ -austenite and δ -ferrite are a double-layer structure. PB has a lower oxidation resistance than austenite and ferrite matrix. The charged H enhances

metal cations (mainly Fe) transport from the substrate to the oxide/solution interface.

2. The δ -ferrite has a higher oxidation resistance than γ -austenite without H. Charged H decreases the oxidation resistance of ferrite and austenite phases. H significantly accelerates the ferrite oxidation due to the internal H diffusion (ferrite acts as the diffusion path for H).
3. H-induced preferential oxidation of GB and penetration oxidation of PB is observed in the H-charged specimen, likely due to the GB and PB act as the H trapping sites.
4. H-assisted SCC cracks initiation and growth of the duplex 308L SS cladding in deaerated high temperature water.

Acknowledgements

This work has been supported by National Key R&D Program of China (No. 2017YFB0703002), Natural Science Foundation of China (NSFC No. 51771107), National Science and Technology Major Project No. 2015ZX06002005.

References

- [1] T. Takeuchi, Y. Kakubo, Y. Matsukawa, Y. Nozawa, T. Toyama, Y. Nagai, Y. Nishiyama, J. Katsuyama, Y. Yamaguchi, K. Onizawa, M. Suzuki, Effects of thermal aging on microstructure and hardness of stainless steel weld-overlay claddings of nuclear reactor pressure vessels, *J. Nucl. Mater.* 452 (2014) 235–240.
- [2] F. Gillemot, M. Horváth, G. Úri, T. Fekete, E. Houndeffo, B. Acosta, L. Debarberis, H.W. Viehrieg, Radiation stability of WWER RPV cladding materials, *Int. J. Press. Ves. Pip.* 84(8) (2007) 469–474.
- [3] B.O. Okonkwo, H. Ming, Z. Zhang, J. Wang, E. Rahimi, S. Hosseinpour, A. Davoodi, Microscale investigation of the correlation between microstructure and galvanic corrosion of low alloy steel A508 and its welded 309/308L stainless steel overlayer, *Corros. Sci.* 154 (2019) 49–60.
- [4] T. Takeuchi, J. Kameda, Y. Nagai, T. Toyama, Y. Matsukawa, Y. Nishiyama, K. Onizawa, Microstructural changes of a thermally aged stainless steel submerged arc weld overlay cladding of nuclear reactor pressure vessels, *J. Nucl. Mater.* 425 (1-3) (2012) 60–64.

- [5] Q. Xiong, H.J. Li, Z.P. Lu, J.J. Chen, Q. Xiao, J.R. Ma, X.K. Ru, Characterization of microstructure of A508III/309L/308L weld and oxide films formed in deaerated high-temperature water, *J. Nucl. Mater.* 498(2018) 227–240.
- [6] T.M. Cui, X.H. Xu, J.R. Ma, Z.P. Lu, Y.J. Tang, K. Zhang, S.L. Yang, Z.M. Zhong, S. Lozano-Perez, T. Shoji, Effects of composition and microstructure on oxidation and stress corrosion cracking susceptibility of stainless steel claddings in hydrogenated PWR primary water, *J. Nucl. Mater.* 553(2021)153057.
- [7] J.A. Brooks, A.W. Thompson, Microstructural development and solidification cracking susceptibility of austenitic stainless steel welds, *Int. Mater. Rev.* 36 (1991) 16–44.
- [8] H.F. Jackson, C.S. Marchi, D.K. Balch, B.P. Somerday, Effect of low temperature on hydrogen-assisted crack propagation in 304L/308L austenitic stainless steel fusion welds, *Corros. Sci.* 77 (2013) 210–221.
- [9] L.E. Thomas, S.M. Bruemmer, High-resolution characterization of intergranular attack and stress corrosion cracking of Alloy 600 in high-temperature primary water, *Corrosion* 56 (2000) 572–587.
- [10] T. Terachi, K. Fujii, K. Arioka, Microstructural characterization of SCC crack tip and oxide film for SUS 316 stainless steel in simulated PWR primary water at 320°C, *J. Nucl. Sci. Technol.* 42 (2005) 225–232.
- [11] K. Fukuya, H. Nishioka, K. Fujii, Y. Kitsunai, Characterization of IASCC crack tip in highly irradiated stainless steels, in: 14th International Conference on Environmental Degradation of Materials in Nuclear Power Systems, Virginia Beach, VA, August 23–27, 2 (2009) 1248–1258.
- [12] M. Meisnar, M. Moody, S.L. Perez, Atom probe tomography of stress corrosion crack tips in SUS316 stainless steels, *Corros. Sci.* 98 (2015) 661–671.
- [13] M. Sennour, P. Laghoutaris, C. Guerre, R. Molins, Advanced TEM characterization of stress corrosion cracking of Alloy 600 in pressurized water reactor primary water environment, *J. Nucl. Mater.* 393 (2009) 254–266.
- [14] P.L. Andresen, M.M. Morra, Stress corrosion cracking of stainless steels and nickel alloys in high-temperature water, *Corrosion* 64 (2008) 15–29.
- [15] T. Shoji, Z.P. Lu, H. Murakami, Formulating stress corrosion cracking growth rates by

- combination of crack tip mechanics and crack tip oxidation kinetics, *Corros. Sci.* 52 (2010) 769–779.
- [16] Z.P. Lu, T. Shoji, H. Xue, C.Y. Fu, Deterministic formulation of the effect of stress intensity factor on PWSCC of Ni-base alloys and weld metals, *J. Press. Vessel Technol.* 135 (2013) 21402-1–9.
- [17] T. Dan, T. Shoji, Z. Lu, K. Sakaguchi, J. Wang, E.H. Han, W. Ke, Effects of hydrogen on the anodic behavior of Alloy 690 at 60°C, *Corros. Sci.* 52(4) (2010) 1228–1236.
- [18] M. Osawa, M. Hasegawa, Stress corrosion cracking of hydrogen-containing austenitic stainless steel in H₂SO₄-NaCl solution, *Trans. ISIJ.* 21(7) (1981) 464–468.
- [19] S. Ningshen, U.K. Mudali, G. Amarendar, P. Gopalan, R.K. Dayal, H.S. Khatak, Hydrogen effects on the passive film formation and pitting susceptibility of nitrogen containing type 316L stainless steels, *Corros. Sci.* 48 (2006) 1106–1121.
- [20] J.J. Chen, Z.P. Lu, F.J. Meng, X.L. Xu, Q. Xiao, H.S. Kim, C. Jang, The corrosion behaviour of alloy 690 tube in simulated PWR secondary water with the effect of solid diffusing hydrogen, *J. Nucl. Mater.* 517 (2019) 179–191.
- [21] S. Thomas, G. Sundararajan, P.D. White, N. Birbilis, The effect of absorbed hydrogen on the corrosion of steels: review, discussion, and implications, *Corrosion* 73(4) (2017) 426–436.
- [22] T.M. Cui, J.R. Ma, K. Zhang, Z.P. Lu, Y.J. Tang, X.H. Xu, S.L. Perez, T. Shoji, Synergistic effect of solid state hydrogen and cold work pretreatment on oxide films grown on 316L stainless steel during short term immersion in deaerated high temperature water at 300 °C, *J. Electrochem. Soc.* 167(16)(2020) 161502.
- [23] L. Qiao, X. Mao, W. Chu, The role of hydrogen in stress-corrosion cracking of austenitic stainless steel in hot MgCl₂ solution, *Metall. Mater. Trans. A* 26A (1995) 1777–1784.
- [24] L.J. Qiao, W.Y. Chu, H.J. Miao, J.M. Xiao, P.X. Guo, Hydrogen-facilitated corrosion and stress corrosion cracking of austenitic stainless steel of type 310, *Metall. Trans. A* 24A (1993) 959–962.

- [25] D.G. Ulmer, C.J. Altstetter, Hydrogen-induced strain localization and failure of austenitic stainless steels at high hydrogen concentrations, *Acta Metall. Mater.* 39(6) (1991) 1237–1248.
- [26] L.J. Qiao, J.L. Luo, Hydrogen-facilitated anodic dissolution of austenitic stainless steels, *Corrosion* 54(4) (1998) 281–288.
- [27] Z. Zhang, J. Tan, X. Wu, E.H. Han, W. Ke, J. Rao, Corrosion fatigue behavior and crack-tip characteristic of 316LN stainless steel in high-temperature pressurized water, *J. Nucl. Mater.* 518 (2019) 21–29.
- [28] J. Lufrano, P. Sofronis, H. K. Birnbaum, Modeling of hydrogen transport and elastically accommodated hydride formation near a crack tip, *J. Mech. Phys. Solids*, 44 (1996) 179–205.
- [29] T.P. Perng, M. Johnson, C. J. Altstetter, Influence of plastic deformation on hydrogen diffusion and permeation in stainless steels, *Acta metall.* 37(12) (1989) 3393–3397.
- [30] W.J. Mills, M.R. Lebo, J.J. Kearns, Hydrogen embrittlement, grain boundary segregation, and stress corrosion cracking of alloy X-750 in low- and high-temperature water, *Metall. Mater. Trans. A* 30A (1999) 1579–1596.
- [31] V. Olden, C. Thaulow, R. Johnsen, Modelling of hydrogen diffusion and hydrogen induced cracking in supermartensitic and duplex stainless steels, *Mater. Des.* 29(10) (2008) 1934–1948.
- [32] T. Mente, T. Boellinghaus, Modeling of hydrogen distribution in a duplex stainless steel, *Weld. World.* 56 (2012) 66–78.
- [33] N.K. Das, K. Suzuki, K. Ogawa, T. Shoji, Early stage SCC initiation analysis of fcc Fe–Cr–Ni ternary alloy at 288 °C: A quantum chemical molecular dynamics approach, *Corros. Sci.* 51 (2009) 908–913.
- [34] B.T. Lu, L.J. Qiao, J.L. Luo, K.W. Gao, Role of hydrogen in stress corrosion cracking of austenitic stainless steels, *Philos. Mag.* 91(2) (2010) 208–228.
- [35] C.D. Beachem, A new model for hydrogen-assisted cracking (hydrogen “embrittlement”), *Metall. Mater. Trans. B* 3(2) (1972) 441–455.
- [36] T. Cui, F. Ning, J. Ma, Z. Lu, K. Zhang, Y. Jia, X. Liang, X. Ru, T. Shoji, Local oxidation penetration of hydrogen-charged 308L stainless steel cladding in deaerated PWR

- primary water, in: Proc. 19th International Conference on Environmental Degradation of Materials in Nuclear Power System-Water Reactors. 2019, 750–764.
- [37] E. Owczarek, T. Zakroczyński, Hydrogen transport in a duplex stainless steel, *Acta Mater.* 48 (2000) 3059–3070.
- [38] Z. Zhang, G. Obasi, R. Morana, M. Preuss, Hydrogen assisted crack initiation and propagation in a nickel-based superalloy, *Acta Mater.* 113 (2016) 272–283.
- [39] P. Reccagni, L.H. Guilherme, Q. Lu, M.F. Gittos, D.L. Engelberg, Reduction of austenite-ferrite galvanic activity in the heat-affected zone of a Gleeble-simulated grade 2205 duplex stainless steel weld, *Corros. Sci.* 161 (2019) 108198.
- [40] K. Kruska, S. Lozano-Perez, D.W. Saxey, T. Terachi, T. Yamada, G.D.W. Smith, Nanoscale characterisation of grain boundary oxidation in cold-worked stainless steels, *Corros. Sci.* 63 (2012) 225–233.
- [41] R.N. Gunn, *Duplex Stainless Steels: Microstructure, Properties and Applications*, 6-Corrosion, Woodhead Publishing, (1997) 73–91.
- [42] P. Williams, R. Faulkner, Chemical volume diffusion coefficients for stainless steel corrosion studies, *J. Mater. Sci.* 22(10) (1987) 3537–3542.
- [43] M.A.E. Jepson, R. L. Higginson, In situ observation of the oxidation of S32101 duplex stainless steel at 900 °C, *Corros. Sci.* 59(2012) 263–269.
- [44] T.M. Cui, Q. Xiong, J.R. Ma, K. Zhang, Z.P. Lu, J.J. Chen, Y.B. Jia, H. Zheng, S.L. Yang, Z.M. Zhong, S. Lozano-Perez, T. Shoji, Oxidation resistance and stress corrosion cracking susceptibility of 308L and 309L stainless steel cladding layers in simulated PWR primary water, *Corrosion* (2021). doi: <https://doi.org/10.5006/3699>
- [45] K. Chen, J. Wang, Z. Shen, D. Du, X. Guo, L. Zhang, P. L. Andresen, Effect of intergranular carbides on the cracking behavior of cold worked alloy 690 in subcritical and supercritical water, *Corros. Sci.* 164 (2020) 108313.
- [46] C. Lai, W. Lu, J. Huang, Effect of δ -ferrite content on the stress corrosion cracking behavior of cast austenitic stainless steel in high-temperature water environment, *Corrosion* 70 (2014) 591–597.

- [47] J. Qian, C.F. Chen, H.B. Yu, F. Liu, H. Yang, Z.H. Zhang, The influence and the mechanism of the precipitate/austenite interfacial C-enrichment on the intergranular corrosion sensitivity in 310 S stainless steel, *Corros. Sci.* 111 (2016) 352–361.
- [48] Y. Fukai, *The metal-hydrogen system*, Springer-Verlag Berlin Heidelberg, Chap. 3, (1993) 95.
- [49] N.K. Das, T. Shoji, An atomic study of hydrogen effect on the early stage oxidation of transition metal surfaces, *Int. J. Hydrogen. Energ.* 38(3) (2013) 1644–1656.
- [50] R. Nishimura, The effect potential on stress corrosion cracking of type 316 and type 310 austenitic stainless steels, *Corros. Sci.* 34(9) (1993) 1463–1473.
- [51] D. Delafosse, T. Magnin, Hydrogen induced plasticity in stress corrosion cracking of engineering systems, *Eng. Fract. Mech.* 68(2001)693-729.
- [52] F.P. Ford, Quantitative prediction of environmentally assisted cracking, *Corrosion* 52 (1996) 375–395.
- [53] P.L. Andresen, F.P. Ford, Life prediction by mechanistic modeling and system monitoring of environmental cracking of iron and nickel alloys in aqueous systems, *Mater. Sci. Eng. A* 103 (1988) 167–184.
- [54] Z.P. Lu, T. Shoji, S. Yamazaki, K. Ogawa, Characterization of microstructure, local deformation and microchemistry in Alloy 600 heat-affected zone and stress corrosion cracking in high temperature water, *Corros. Sci.* 58 (2012) 211–228.
- [55] J.J. Chen, Q. Xiao, Z.P. Lu, X.K. Ru, H. Peng, Q. Xiong, H.J. Li, Characterization of interfacial reactions and oxide films on 316L stainless steel in various simulated PWR primary water environments, *J. Nucl. Mater.* 489 (2017) 137–149.
- [56] N. Birks, G.H. Meier, *Introduction to high temperature oxidation of metals*, Edward Arnold Ltd, London, Chap. IV, (1983) 42.
- [57] X. Tao, G.C. Lv, J. Kou, X. Xiong, A. A. Volinsky, C.S. Ku, K. Chen, Y.J. Su, Synchrotron X-ray Laue diffraction study of hydrogen-induced blisters on iron grain boundaries, *Scripta Mater.* 169 (2019) 82–86.

Figure captions

Fig. 1. (a) Sampling location for microstructure analysis and exposure tests, (b) SEM morphologies of 308L SS surface after electro-etched.

Fig. 2. The SEM-EDS area maps and the element profile of the ferrite in 308L SS.

Fig. 3. XRD patterns of the oxide film formed on 308L SS with and without charged-hydrogen after being exposed to deaerated high temperature water at 290 °C for 168 h and 600 h.

Fig. 4. SEM images showing the morphologies of oxide films and ferrites after being exposed to deaerated high temperature water at 290 °C for 168 h: (a) (b) (c) 308-168N, (d) (e) (f) 308-168H.

Fig. 5. TEM-EDS results of the oxide film formed on austenite of 308-168N after being exposed to deaerated high temperature water at 290 °C for 168 h: (a) (b) STEM-HAADF and STEM-BF images of the oxide film formed on austenite and the corresponding EDS area maps, (c) EDS line scan profile shown in (a) as line 1, (d) EDS line scan shown in (a) as line 2.

Fig. 6. TEM results of the sampling location of the phase boundary and the oxide film formed on 308-168N after being exposed to deaerated high temperature water at 290 °C for 168 h: (a) TEM-BF image of the oxide films and phase boundary, (b) STEM-HAADF image of the oxide film formed near the left side phase boundary shown in (a), (c) HRTEM image of the oxide film on ferrite, (d) (e) STEM-HAADF and STEM-BF images of the oxide film formed near the right side phase boundary shown in (a), and the corresponding EDS area maps.

Fig. 7. TEM-EDS results of the oxide film formed on austenite of 308-168H after being exposed to deaerated high temperature water at 290 °C for 168 h: (a) STEM-HAADF image of the oxide films on austenite and the corresponding EDS area maps, (b) STEM-BF image of the oxide films on austenite, (c) EDS line scan profile shown in (a) as line 1, (d) EDS line scan shown in (a) as line 2.

Fig. 8. TEM-EDS results of the sampling location of the phase boundary and the oxide film formed on 308-168H after being exposed to deaerated high temperature water at 290 °C for 168 h: (a) STEM-HAADF image of the oxide films formed near phase boundary and the corresponding EDS area maps, (b) STEM-BF image of the oxide films formed near phase

boundary.

Fig. 9. SEM images showing the morphologies of oxide films and ferrites after being exposed to deaerated high temperature water at 290 °C for 600 h: (a) (b) (c) 308-600N, (d) (e) (f) 308-600H.

Fig. 10. TEM-EDS results of the sampling location of the phase boundary and the oxide film formed on 308-600N after being exposed to deaerated high temperature water at 290 °C for 600 h: (a) STEM-HAADF image of the phase boundary and oxide film, and the corresponding EDS area maps of the rectangular region, (b) EDS line scan across the phase boundary, (c) STEM-HAADF image of the oxide film on austenite, (d) EDS line scan of the oxide film on austenite, (e) STEM-HAADF image of the oxide film on ferrite, (f) EDS line scan of the oxide film on ferrite. [36]

Fig. 11. TEM results of the sampling location of the phase boundary and the oxide film formed on 308-600N after being exposed to deaerated high temperature water at 290 °C for 600 h: (a) TEM-BF image of the austenite/ferrite phases and oxide film, (b) High magnification TEM-BF image of the phase boundary and oxide film, as located in (a) rectangular area. SAED image of the ferrite is shown in (b) as pattern I, SAED image of the outer oxide is shown in (b) as pattern II, SAED image of the carbide is shown in (b) as pattern III, and the diffractions from FFT of the inner oxide is shown in (b) as pattern IV. [36]

Fig. 12. TEM results of the sampling location of the grain boundary and the oxide film formed on 308-600H after being exposed to deaerated high temperature water at 290 °C for 600 h: (a) STEM-HAADF image of the grain boundary and oxide films, and the corresponding EDS area maps of the rectangular region, (b) EDS line scan shown in (a) as line 1, (c) TEM-BF image of the grain boundary and the oxide film on austenite. SAED image of the carbide is shown in (c) as pattern I, SAED image of the outer oxide is shown in (c) as pattern II, SAED image of the inner oxide is shown in (c) as pattern III.

Fig. 13. TEM-EDS results of the sampling location of the phase boundary and the oxide film formed on 308-600H after being exposed to deaerated high temperature water at 290 °C for 600 h: (a) STEM-HAADF image of the sampling location 1 of the phase boundary and the oxide film, and the corresponding EDS area maps, (b) STEM-HAADF image of the sampling location 2 of the phase boundary and the oxide film, (c) EDS line scan profile shown in (a)

as line 1, (d) EDS line scan profile shown in (a) as line 2. [36]

Fig. 14. TEM results of the sampling locations of the phase boundaries and oxide films formed on 308-600H after being exposed to deaerated high temperature water at 290 °C for 600 h: (a) TEM-BF image of the sampling location 1 of the phase boundary and oxide film, (b) TEM-BF image of the sampling location 2 of the phase boundary and oxide film. SAED image of the austenite is shown in (a) as pattern I, SAED image of the ferrite is shown in (a) as pattern II, SAED image of the outer oxide is shown in (a) as pattern III, the diffractions from FFT of the inner oxide is shown in (a) as pattern IV, the SAED image of the inner oxide is shown in (b) as pattern V. [36]

Fig. 15. Stress-strain curves after SSRT test at 3×10^{-7} /s for 308-SN and 308-SH specimens in deaerated high temperature water at 325 °C.

Fig. 16. SEM morphologies of the fracture surface and gauge side after SSRT test at 3×10^{-7} /s for 308-SN specimen in deaerated high temperature water at 325 °C.

Fig. 17. SEM morphologies of the fracture surface and gauge side after SSRT test at 3×10^{-7} /s for 308-SH specimen in deaerated high temperature water at 325 °C.

Fig. 18. Schematic diagrams of the oxidation behaviour of the austenite and ferrite in 308L SS cladding after being exposed to deaerated high temperature water: (a) Non-charged specimen, (b) H-charged specimen.

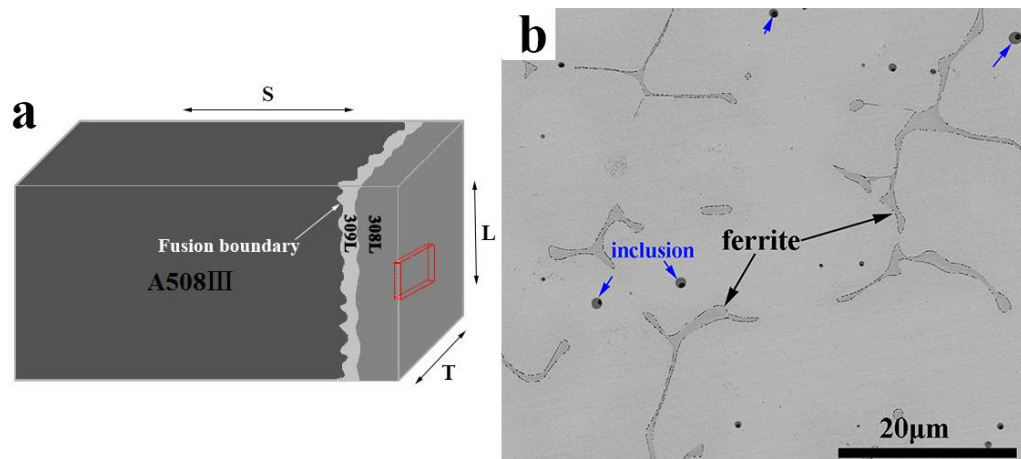


Fig. 1. (a) Sampling location for microstructure analysis and exposure tests, (b) SEM morphologies of 308L SS surface after electro-etched.

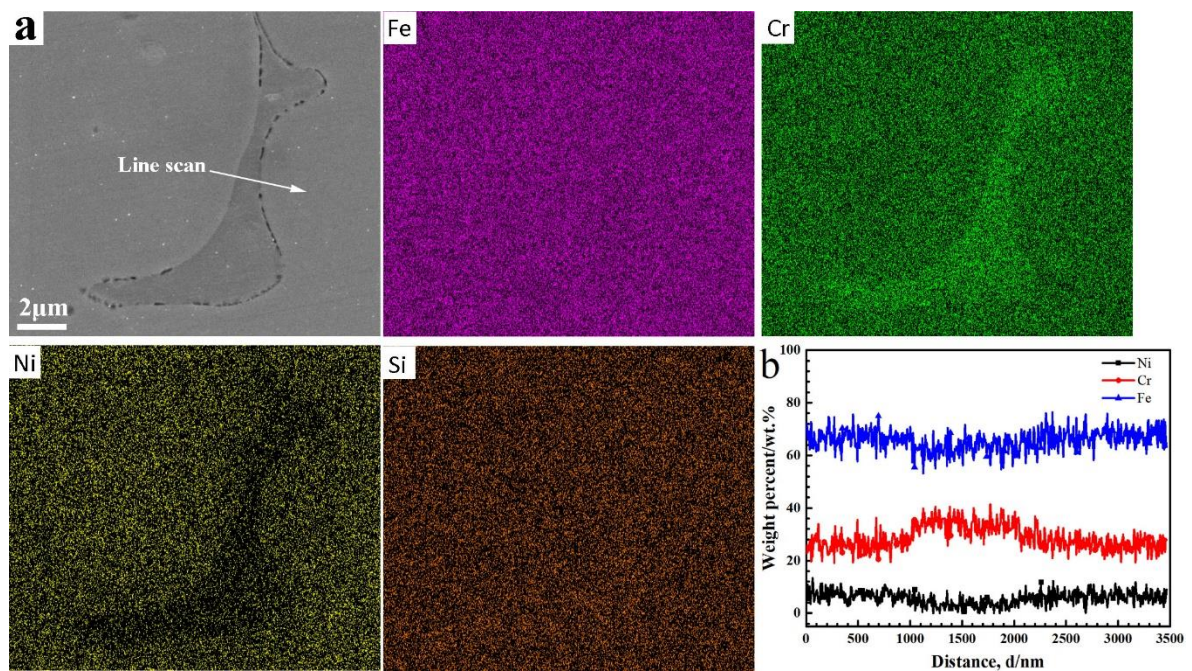


Fig. 2. The SEM-EDS area maps and the element profile of the ferrite in 308L SS.

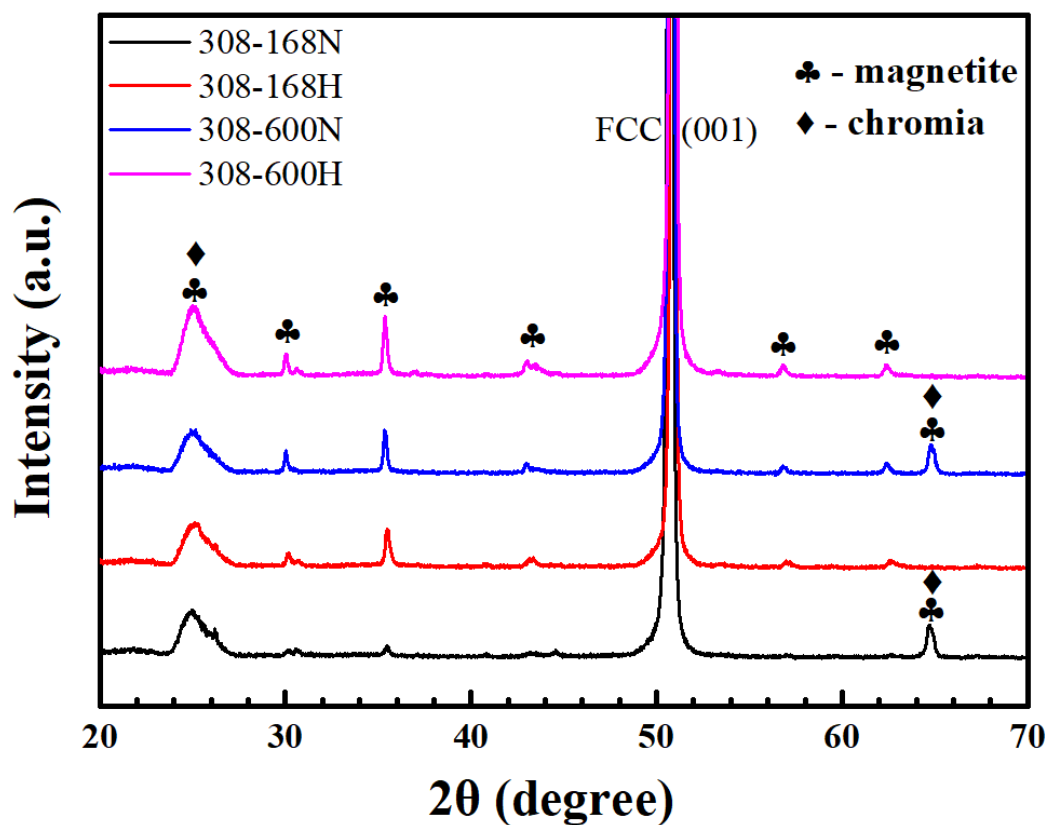


Fig. 3. XRD patterns of the oxide film formed on 308L SS with and without charged-hydrogen after being exposed to deaerated high temperature water at 290 °C for 168 h and 600 h.

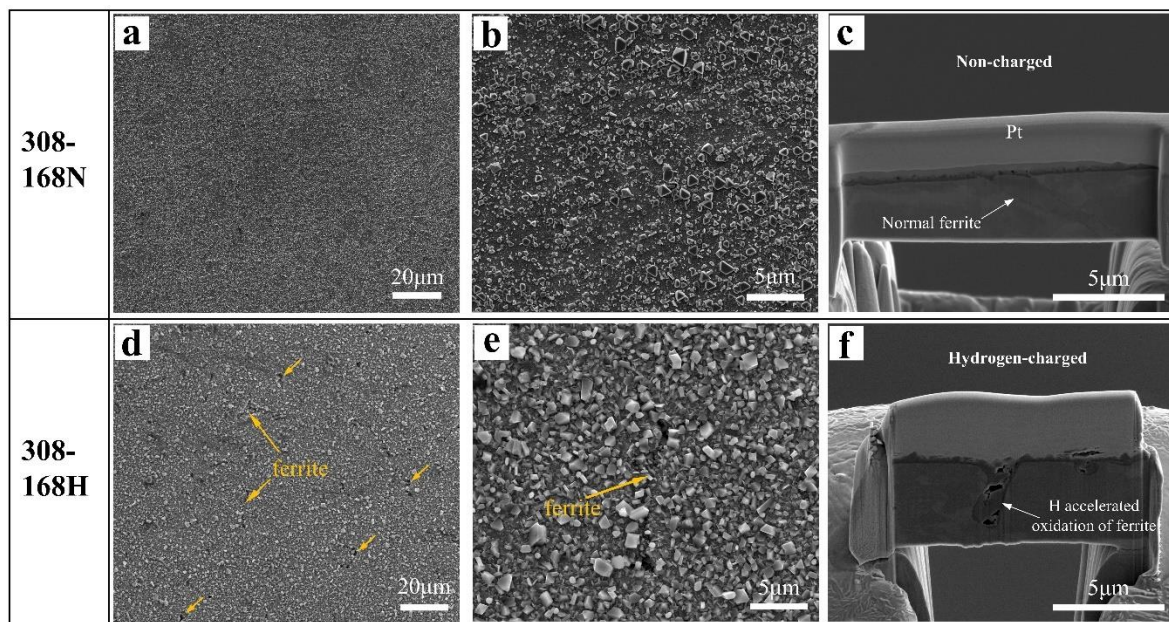


Fig. 4. SEM images showing the morphologies of oxide films and ferrites after being exposed to deaerated high temperature water at 290 °C for 168 h: (a) (b) (c) 308-168N, (d) (e) (f) 308-168H.

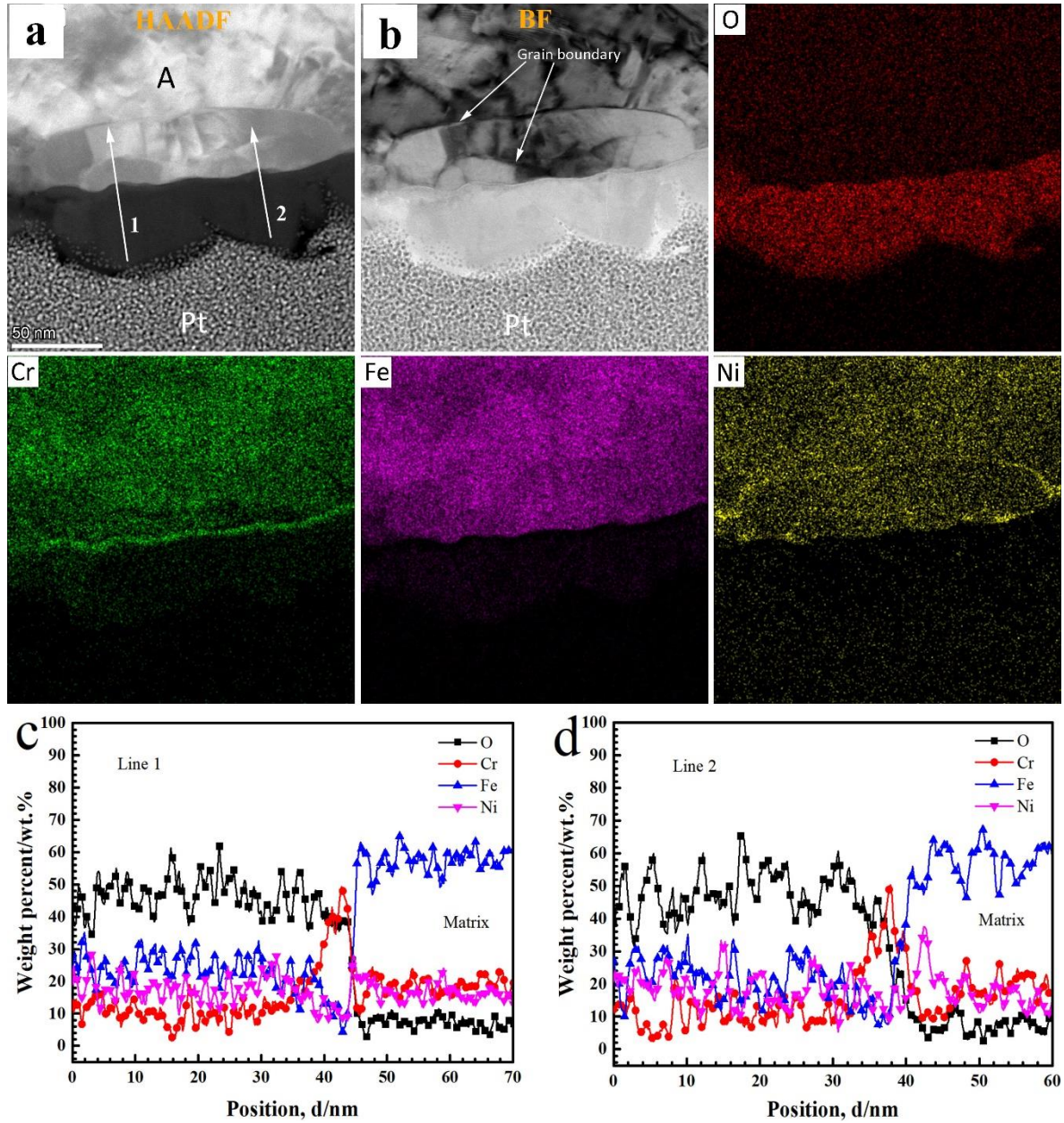


Fig. 5. TEM-EDS results of the oxide film formed on austenite of 308-168N after being exposed to deaerated high temperature water at 290 °C for 168 h: (a) (b) STEM-HAADF and STEM-BF images of the oxide film formed on austenite and the corresponding EDS area maps, (c) EDS line scan profile shown in (a) as line 1, (d) EDS line scan shown in (a) as line 2.

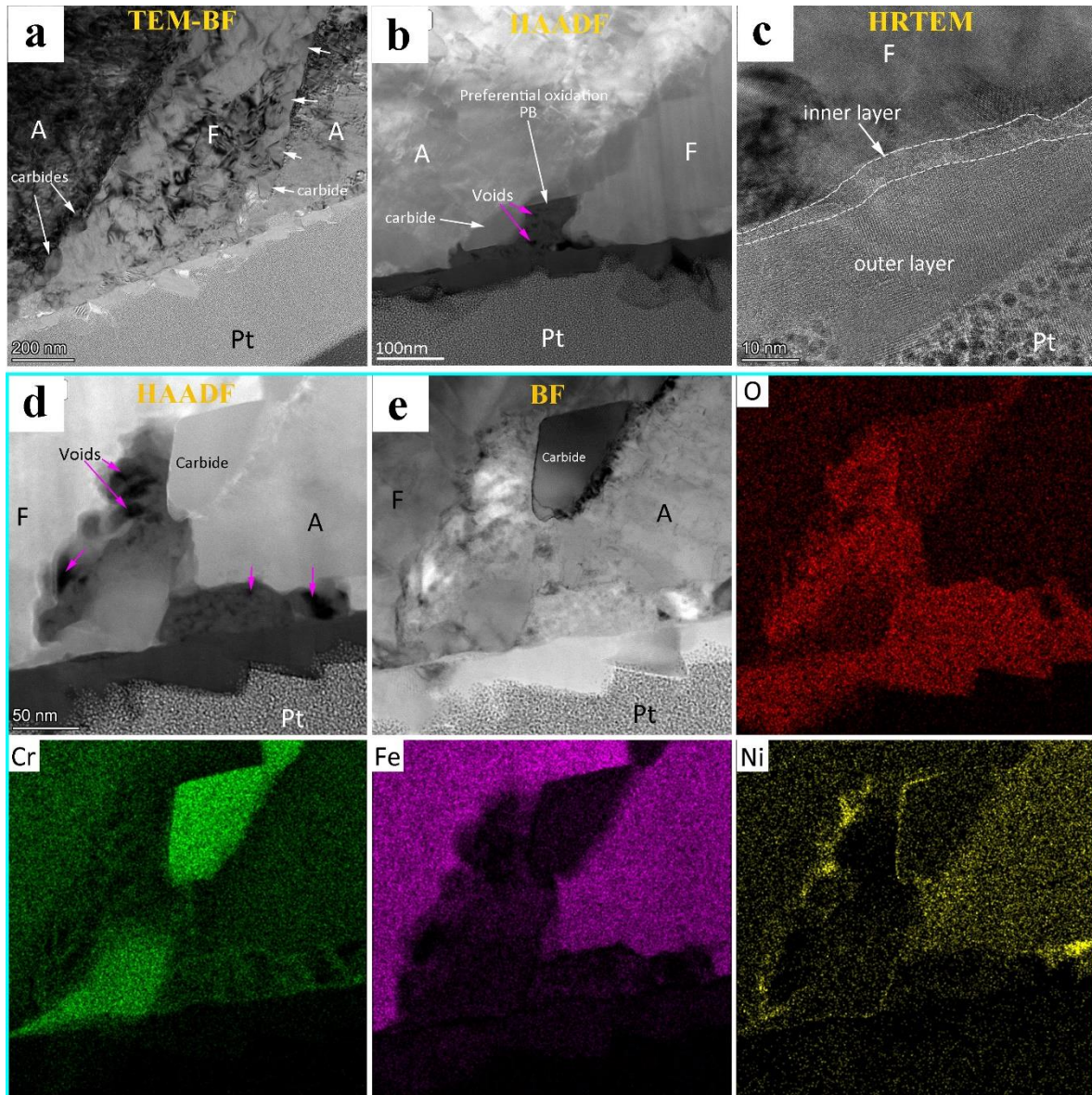


Fig. 6. TEM results of the sampling location of the phase boundary and the oxide film formed on 308-168N after being exposed to deaerated high temperature water at 290 °C for 168 h: (a) TEM-BF image of the oxide films and phase boundary, (b) STEM-HAADF image of the oxide film formed near the left side phase boundary shown in (a), (c) HRTEM image of the oxide film on ferrite, (d) (e) STEM-HAADF and STEM-BF images of the oxide film formed near the right side phase boundary shown in (a), and the corresponding EDS area maps.

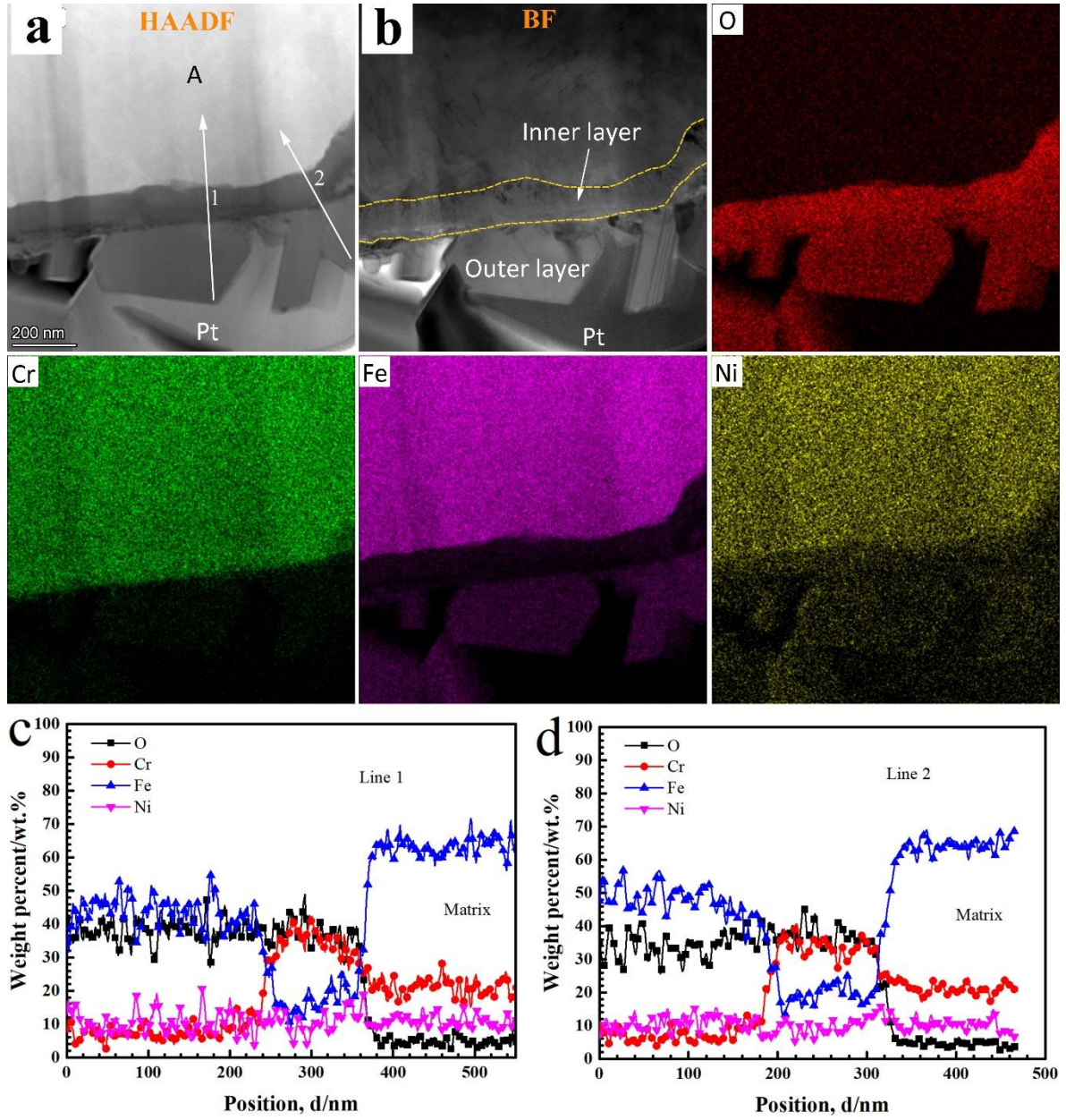


Fig. 7. TEM-EDS results of the oxide film formed on austenite of 308-168H after being exposed to deaerated high temperature water at 290 °C for 168 h: (a) STEM-HAADF image of the oxide films on austenite and the corresponding EDS area maps, (b) STEM-BF image of the oxide films on austenite, (c) EDS line scan profile shown in (a) as line 1, (d) EDS line scan shown in (a) as line 2.

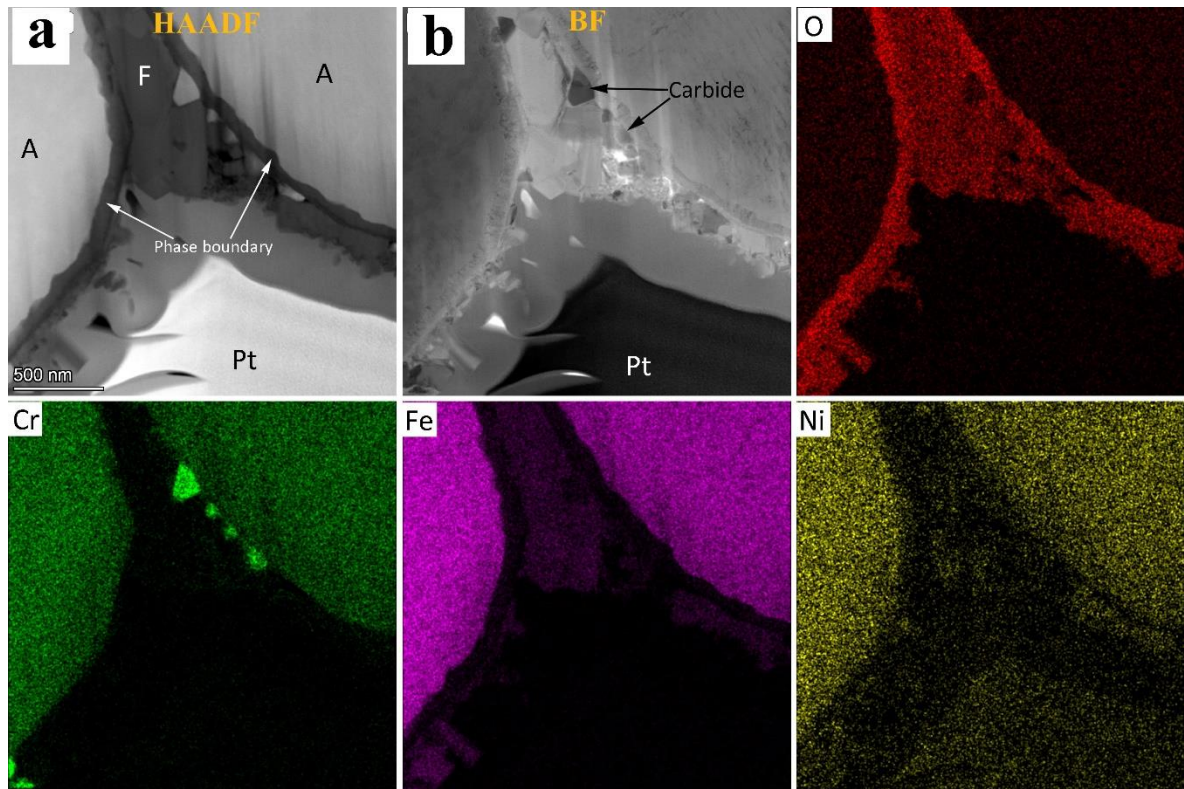


Fig. 8. TEM-EDS results of the sampling location of the phase boundary and the oxide film formed on 308-168H after being exposed to deaerated high temperature water at 290 °C for 168 h: (a) STEM-HAADF image of the oxide films formed near phase boundary and the corresponding EDS area maps, (b) STEM-BF image of the oxide films formed near phase boundary.

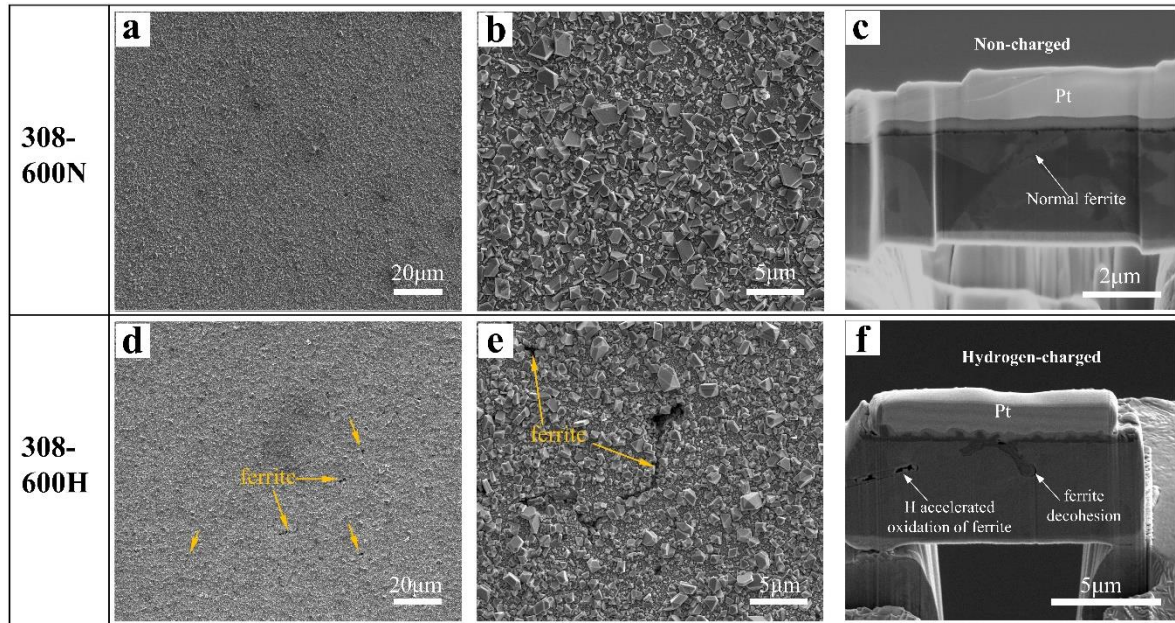


Fig. 9. SEM images showing the morphologies of oxide films and ferrites after being exposed to deaerated high temperature water at 290 °C for 600 h: (a) (b) (c) 308-600N, (d) (e) (f) 308-600H.

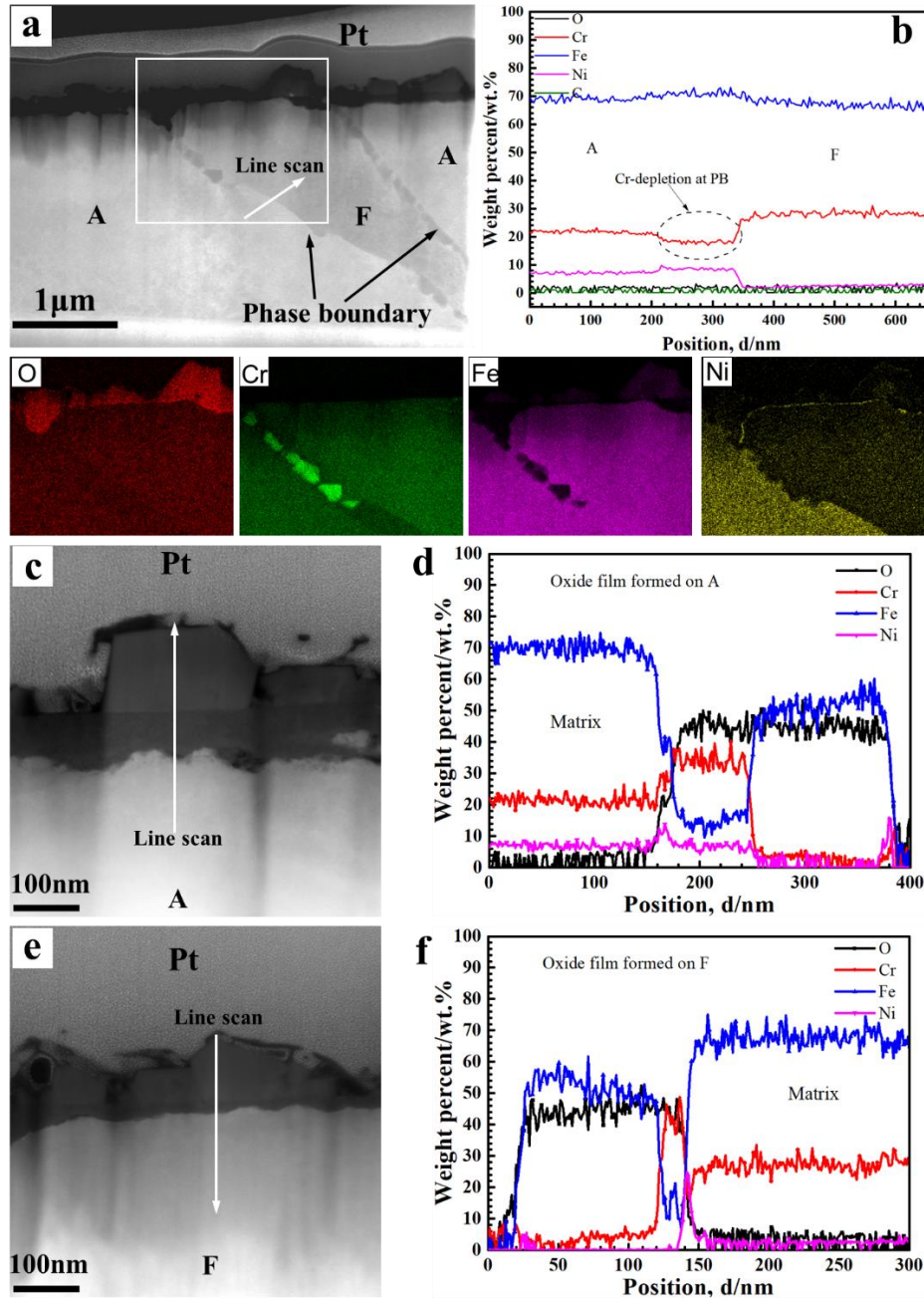


Fig. 10. TEM-EDS results of the sampling location of the phase boundary and the oxide film formed on 308-600N after being exposed to deaerated high temperature water at 290 °C for 600 h: (a) STEM-HAADF image of the phase boundary and oxide film, and the corresponding EDS area maps of the rectangular region, (b) EDS line scan across the phase boundary, (c) STEM-HAADF image of the oxide film on austenite, (d) EDS line scan of the oxide film on austenite, (e) STEM-HAADF image of the oxide film on ferrite, (f) EDS line scan of the oxide film on ferrite. [36]

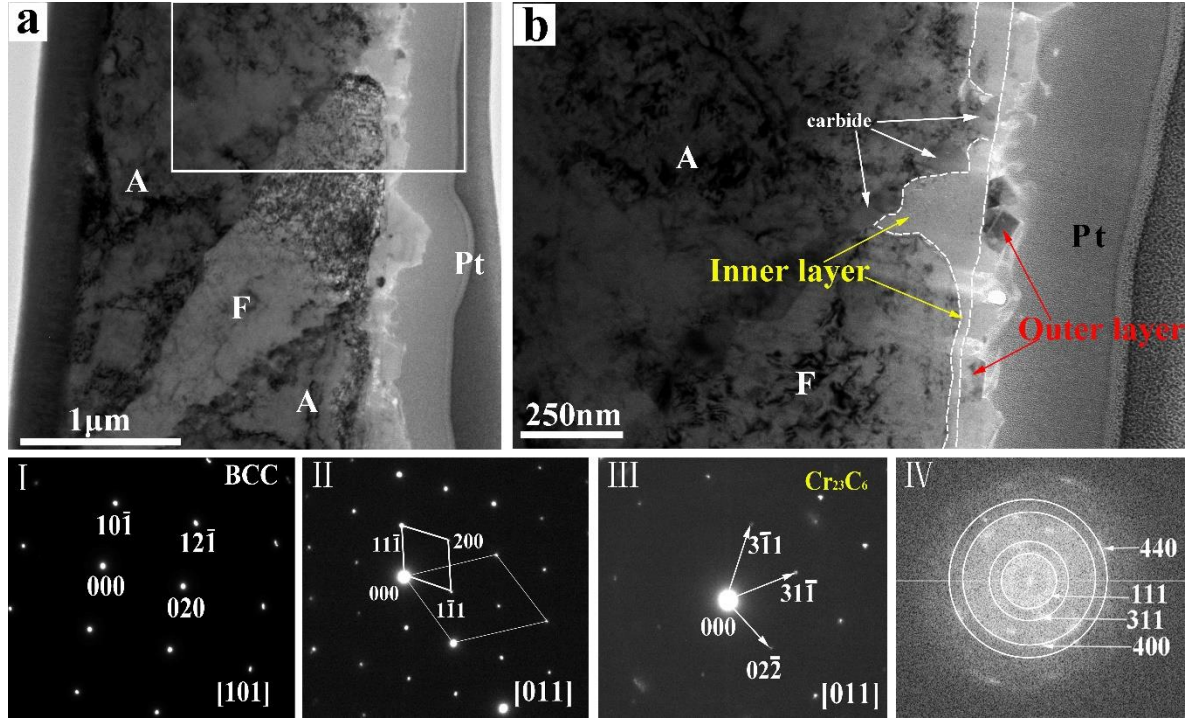


Fig. 11. TEM results of the sampling location of the phase boundary and the oxide film formed on 308-600N after being exposed to deaerated high temperature water at 290 °C for 600 h: (a) TEM-BF image of the austenite/ferrite phases and oxide film, (b) High magnification TEM-BF image of the phase boundary and oxide film, as located in (a) rectangular area. SAED image of the ferrite is shown in (b) as pattern I, SAED image of the outer oxide is shown in (b) as pattern II, SAED image of the carbide is shown in (b) as pattern III, and the diffractions from FFT of the inner oxide is shown in (b) as pattern IV. [36]

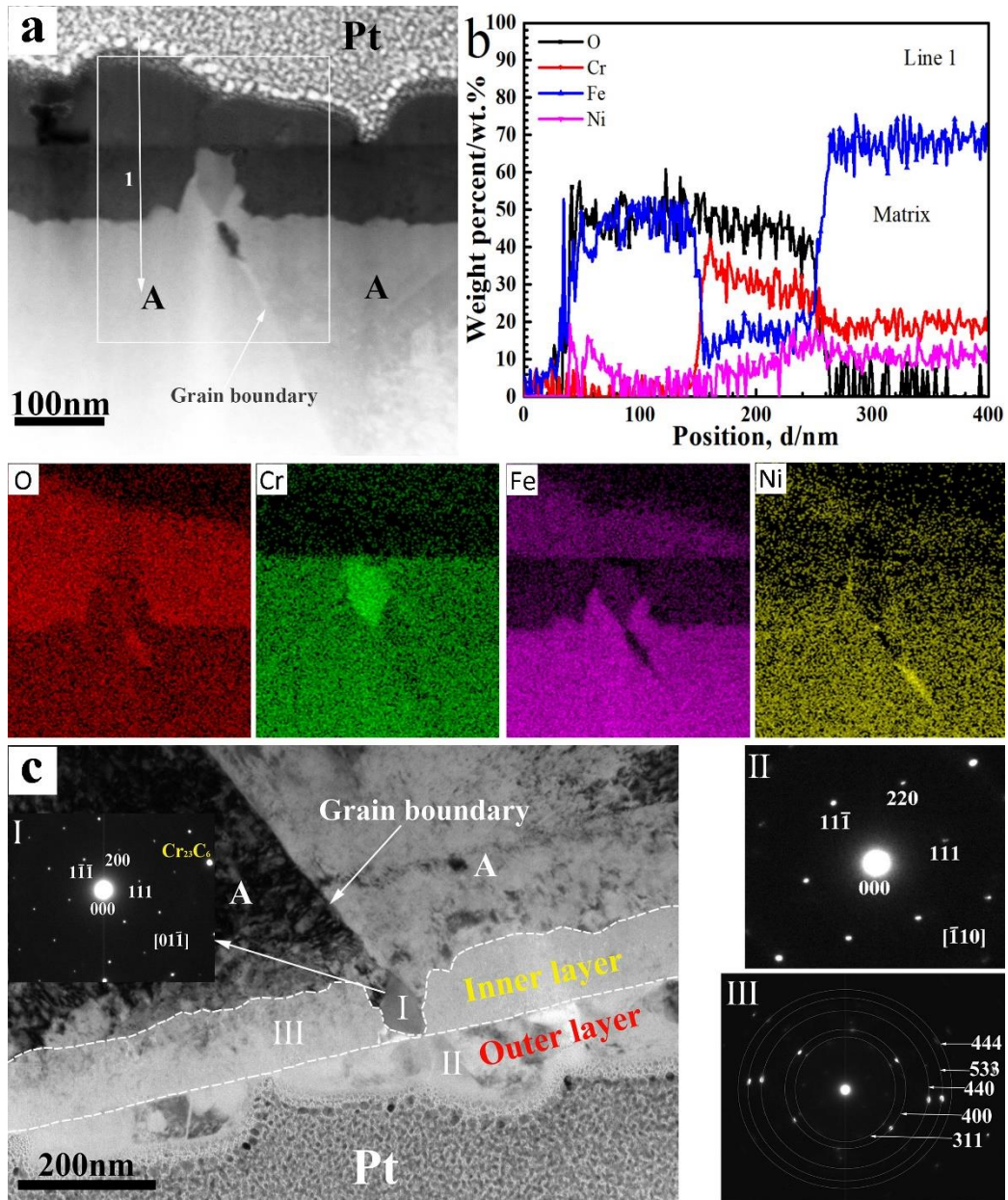


Fig. 12. TEM results of the sampling location of the grain boundary and the oxide film formed on 308-600H after being exposed to deaerated high temperature water at 290 °C for 600 h: (a) STEM-HAADF image of the grain boundary and oxide films, and the corresponding EDS area maps of the rectangular region, (b) EDS line scan shown in (a) as line 1, (c) TEM-BF image of the grain boundary and the oxide film on austenite. SAED image of the carbide is shown in (c) as pattern I, SAED image of the outer oxide is shown in (c) as pattern II, SAED image of the inner oxide is shown in (c) as pattern III.

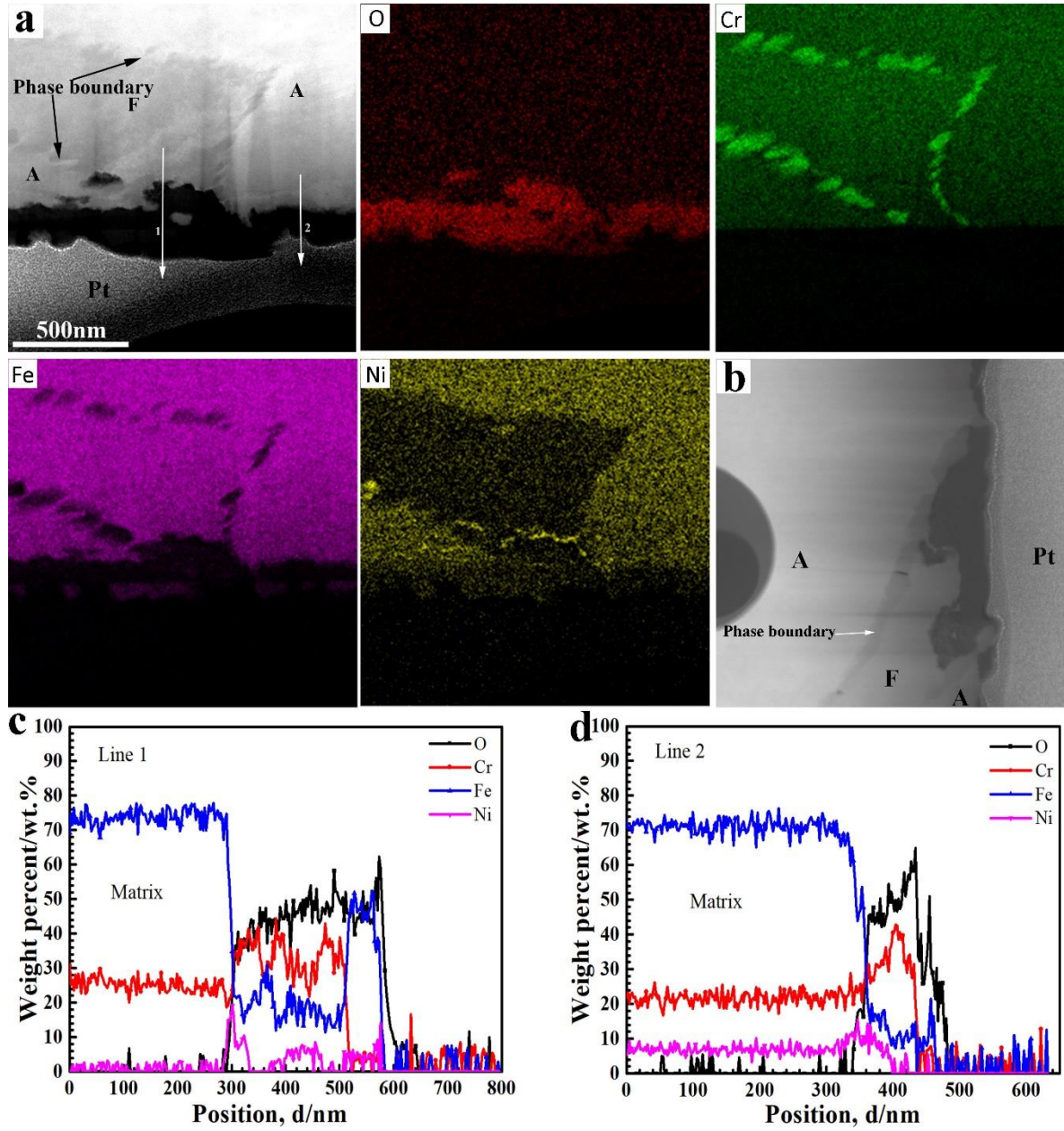


Fig. 13. TEM-EDS results of the sampling location of the phase boundary and the oxide film formed on 308-600H after being exposed to deaerated high temperature water at 290 °C for 600 h: (a) STEM-HAADF image of the sampling location 1 of the phase boundary and the oxide film, and the corresponding EDS area maps, (b) STEM-HAADF image of the sampling location 2 of the phase boundary and the oxide film, (c) EDS line scan profile shown in (a) as line 1, (d) EDS line scan profile shown in (a) as line 2. [36]

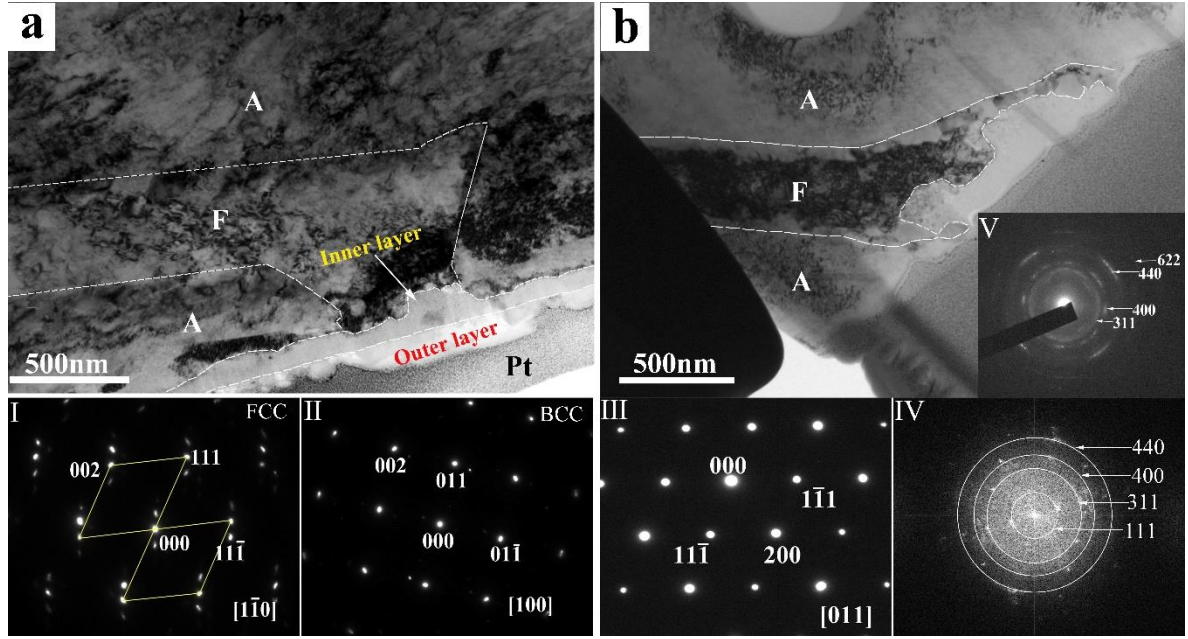


Fig. 14. TEM results of the sampling locations of the phase boundaries and oxide films formed on 308-600H after being exposed to deaerated high temperature water at 290 °C for 600 h: (a) TEM-BF image of the sampling location 1 of the phase boundary and oxide film, (b) TEM-BF image of the sampling location 2 of the phase boundary and oxide film. SAED image of the austenite is shown in (a) as pattern I, SAED image of the ferrite is shown in (a) as pattern II, SAED image of the outer oxide is shown in (a) as pattern III, the diffractions from FFT of the inner oxide is shown in (a) as pattern IV, the SAED image of the inner oxide is shown in (b) as pattern V. [36] □

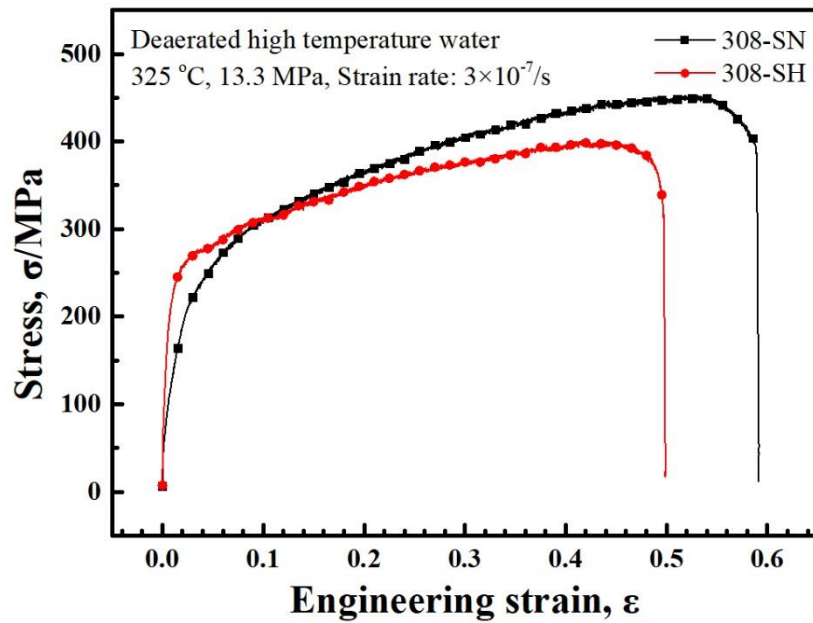


Fig. 15. Stress-strain curves after SSRT test at 3×10^{-7} /s for 308-SN and 308-SH specimens in deaerated high temperature water at 325 °C.

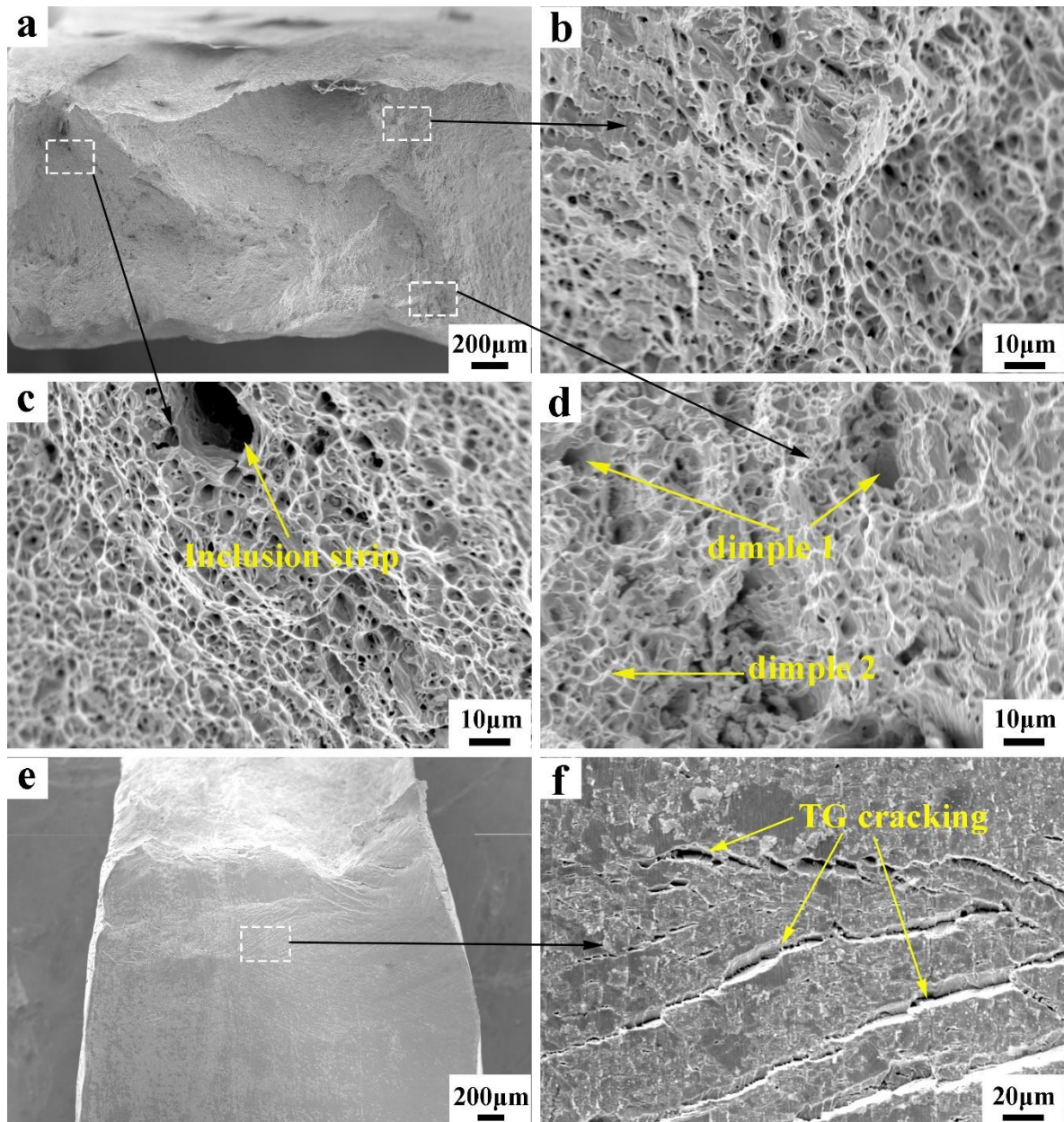


Fig. 16. SEM morphologies of the fracture surface after SSRT test at 3×10^{-7} /s for 308-SN specimen in deaerated high temperature water at 325 °C.

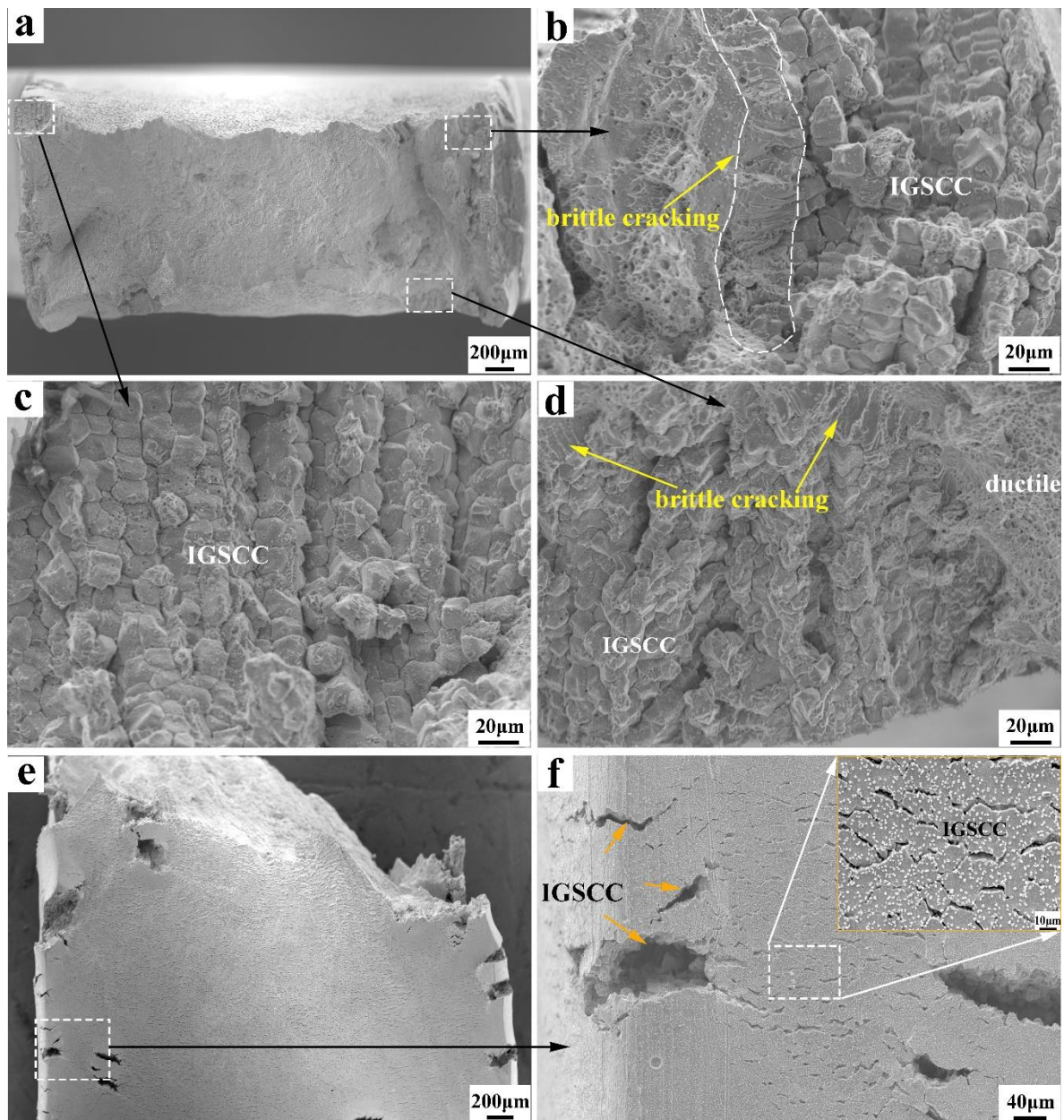


Fig. 17. SEM morphologies of the fracture surface after SSRT test at 3×10^{-7} /s for 308-SH specimen in deaerated high temperature water at 325 °C.

